SOFC composite cathodes based on LSM and co-doped cerias ($Ce_{0.8}Gd_{0.1}X_{0.1}O_{2−\delta}$, X = Gd, Cr, Mg, Bi, Ce)

M. Balaguer, V.B. Vert [1], L. Navarrete, J.M. Serra*

Instituto de Tecnología Química (Universidad Politécnica de Valencia − Consejo Superior de Investigaciones Científicas), Av. Los Naranjos, s/n, 46022 Valencia, Spain

HIGHLIGHTS

► Composite SOFC cathodes were prepared by mixing LSM and multidoped ceria.
► Total conductivity and electrode polarization were measured and correlated.
► Impedance analysis allowed distinguishing three different electrode contribution.
► The best cathode contained Mg and Gc co-doped ceria mixed with LSM.

ARTICLE INFO

ABSTRACT

Ceria-based materials have been incorporated into LSM conventional cathodes in order to improve the electrochemical performance. Gadolinium and other elements (Mg, Cr and Bi) have been used as ceria co-dopants in order to enhance conduction and electrocatalytic properties of several LSM-ceria composites. Among the different tested LSM-ceria cathodes, $Ce_{0.8}Gd_{0.1}Mg_{0.1}O_{2−\delta}$-based composite material offers the lowest electrode polarization resistance in the 700–900 °C temperature range. However, at the lowest tested temperatures these results are similar to those obtained for the $Ce_{0.8}Gd_{0.2}O_{2−\delta}$ binary system, thus the selection of Gd-co-doping elements should principally address economic issues. Since LSM-based cathodes are pointed for high temperature applications (>800 °C), this magnesium-co-doped ceria-gadolinia compound could be an alternative to the widely used $Ce_{1−x}Gd_xO_{2−\delta}$ binary system.

1. Introduction

Strontium doped lanthanum manganite ($La_{1−x}Sr_xMnO_3$ − LSM) perovskites are the principal component of the state-of-the-art materials for SOFC cathodes [1]. LSM-based compositions showed interesting electrochemical properties for oxygen activation at high temperatures while they are thermo-chemically compatible with the widely used YSZ electrolyte material. However, the lack of ionic conductivity and the decreasing performance of LSM cathodes at temperatures below 800 °C require mixing the LSM with electrolyte materials. These LSM-electrolyte composites allow increasing the global ionic conductivity of the cathode while augments the three-phase-boundary (TPB) region thus enhancing the cathode performance. In order to increase the electrochemical performance of LSM-based composite cathodes it is desirable that the electrolyte-like component possesses high oxygen ion conductivity, some electronic paths and/or enhanced catalytic activity for the oxygen reduction reaction at the operating temperature.

Rare earth-doped cerias show high ionic conductivity [2] and interesting catalytic redox properties. Gadolinia doped ceria oxide (GDC) seems to be an interesting electrolyte material since it has higher ionic [3] conductivity than YSZ electrolyte, specifically at low temperatures. In addition, thermo-chemical properties of GDC material fit much closer with LSM than YSZ electrolytes [4]. The presence of gadolinium favors the oxygen ion conductivity and the addition of other doping elements may promote electronic conductivity [5]. Moreover, the use of doped cerias in composite cathodes allows incorporating additional redox electrocatalytic activity [6,7], with regard to the YSZ-based cathodes. However, the combined use of

* Corresponding author. Tel.: +34 963879448; fax: +34 963877809.
  E-mail address: jmserra@itq.upv.es (J.M. Serra).
[1] Present address: Centro Nacional de Experimentación de Tecnologías de Hidrógeno y Pilas de Combustible, Prolongación de Fernando el Santo, s/n, 13500 Puertollano, Ciudad Real, Spain.

GDC and YSZ requires the limitation of final firing temperatures due to the deleterious reaction between both materials.

With this premise, this work shows the electrochemical performance of several LSM composite SOFC cathodes, fabricated with different co-doped gadolinium–cerium oxides based on the $Ce_{0.8}Gd_{0.1}X_{0.1}O_{2-\delta}$ (X = Gd, Cr, Mg, Bi, Ce) nominal formula.

2. Experimental

Different $Ce_{0.8}Gd_{0.1}X_{0.1}O_{2-\delta}$ (X = Gd, Cr, Mg, Bi, Ce) compositions have been synthesized by co-precipitation method in order to synthesize powders of nanometric size. This technique consists of the dissolution of commercial metal nitrates in distilled water at 50 °C. $(NH_4)_2CO_3$ solution, in a 1:1.5 molar ratio, was dropped into the solution to achieve the total precipitation of the mixed cations. The resulting precursor powders were dried at 100 °C after filtration and rinsing with water. Finally, each powder was calcined during 5 h in air at 800 °C to decompose the residual nitrates and carbonates, and to favour the formation of the fluorite phase. $La_{0.8}Sr_{0.2}MnO_3$ (LSM) powder was commercially available (Fuel Cell Materials – USA).

To identify the crystalline phase and determine size and lattice parameters of the different materials, the powders were characterized by X-ray diffraction (XRD). Measurements were carried out in a PANalytical Cubix fast diffractometer by using $CuK_{\alpha1,2}$ radiation, and an X'Celerator detector in Bragg-Brentano geometry. XRD patterns were recorded in the 2θ range from 0° to 90° and analyzed using the X'Pert HighScore Plus [8] software.

Electrical conductivity measurements were conducted by standard four-point DC technique on sintered rectangular prisms. As-calcined powders were uniaxially pressed in rectangular prisms ($4 \times 0.4 \times 0.2$ cm^3) at 125 MPa and sintered for 5 h at 1300 °C, achieving very high (>99%) density. Measurements were carried out in the 400–800 °C temperature range by cooling down (1 K min^{-1}) in given O_2-containing atmospheres (Linde calibrated gas mixtures were checked by an YSZ oxygen sensor). Current was supplied by a Keithley 2601 programmable current source and voltage drop through the sample was detected by a Keithley 3706 multimeter. The samples were stabilized for 2 h at 800 °C prior to conductivity measurements in order to guarantee the high temperature reduction state corresponding to the specific pO_2.

Screen-printing inks made of composite cathodes were prepared by mixing in a three roll mill LSM, the corresponding ceria-based material and a ethylcellulose (6% wt.) solution in terpineol. The final weight ratio among these three components was 1:1:2. These inks were applied on both sides of $Ce_{0.8}Gd_{0.2}O_{2-\delta}$ (with 2%wt. Co) ~1 mm-thick fully-dense [2,9] electrolytes provided by IKTS Fraunhofer (Germany). Porous electrodes were obtained after calcining the resulting screen-printed layers at 1150 °C for 2 h. A top screen-printed gold mesh was applied on the electrodes in order to ensure proper current collection.

As-fabricated symmetrical cells were tested by means of electrochemical impedance spectroscopy measurements using a 0 V DC – 20 mV AC amplitude signal using a Solartron 1470E/1455 FRA device. Electrochemical measurements were performed in air in the 700–900 °C temperature range. Particle size and morphology of the powder samples as well as electrode microstructure was analyzed by SEM imaging in a JEOL 6360 microscope.

3. Results

3.1. Structural characterization: XRD and SEM analysis

Different pure fluorite compounds (Table 1) were synthesized by means of co-precipitation method followed by a firing step air.

Table 1
Cerium-based compositions synthesized as cubic fluorite structure with the nomenclature used along the text, and the corresponding lattice parameter and crystallite size extracted from XRD patterns.

Composition	Nomenclature	Lattice parameter (Å)	Crystallite size (Å)
$Ce_{0.8}Gd_{0.2}O_{2-\delta}$	CG82	5.4224	529
$Ce_{0.9}Gd_{0.1}O_{2-\delta}$	CG91	5.4152	535
$Ce_{0.8}Gd_{0.1}Bi_{0.1}O_{2-\delta}$	CGBi	5.4153	255
$Ce_{0.8}Gd_{0.1}Cr_{0.1}O_{2-\delta}$	CGCr	5.4143	169
$Ce_{0.8}Gd_{0.1}Mg_{0.1}O_{2-\delta}$	CGMg	5.4159	477

These compositions comprise both CG82 and CG91 parent materials and also the corresponding magnesium-, bismuth- and chromium-co-doped materials.

Fig. 1 plots the XRD patterns of the powders sintered at 800 °C showing the expected cubic fluorite structure. Diffraction peaks corresponding to any other oxide or any precursor are not observed, which means that the different dopants are fully incorporated into the ceria lattice. Crystallographic lattice parameters (a) for the (h k l) planes were calculated using the corresponding equation for a cubic system and the results are summarized in Table 1. Crystallite sizes were extracted by fitting the (422) plane reflection to a Gaussian function [10]. The small amount of the co-dopant has small influence on the lattice size, calculated from the XRD patterns (Table 1), but it seems to have some effect on the ceria crystallite size as determined by SEM analysis. Indeed, by using the same synthesis method it is possible to obtain a range of crystallite sizes depending on the co-doping added element. Further investigations should be focused on this fact, studying the nucleation and crystal growth during precipitation and later sintering process, and its ultimate influence on crystallite size. Fig. S1 illustrates the effect of Cr addition, which reduces the sintering activity of Gd-doped ceria. Consequently, the dopant incorporation may induce changes not only on bulk transport (ionic and electronic) and specific reaction rate but also on the electrode microstructure.

Irrespective of differences in crystallite size among co-doping elements (Table 1), co-precipitation synthesis method permits obtaining powders with nanometric particles, as observed in
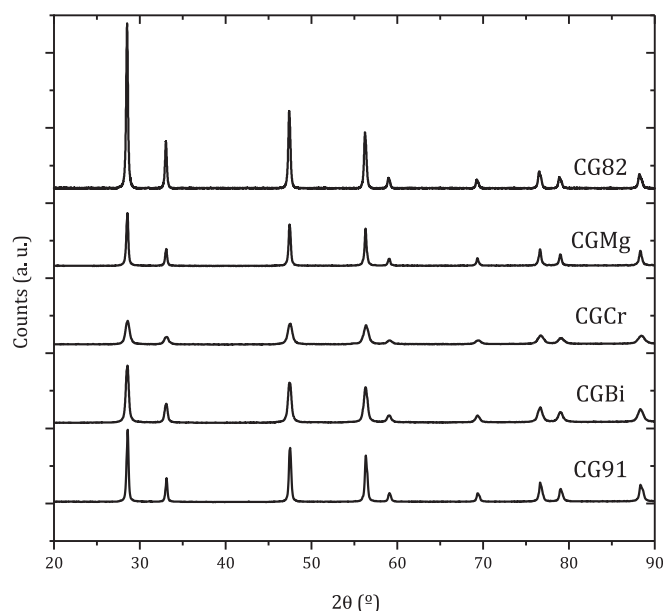

Fig. 1. Room temperature X-ray diffraction patterns of the as-sintered doped cerias after 800 °C calcination.
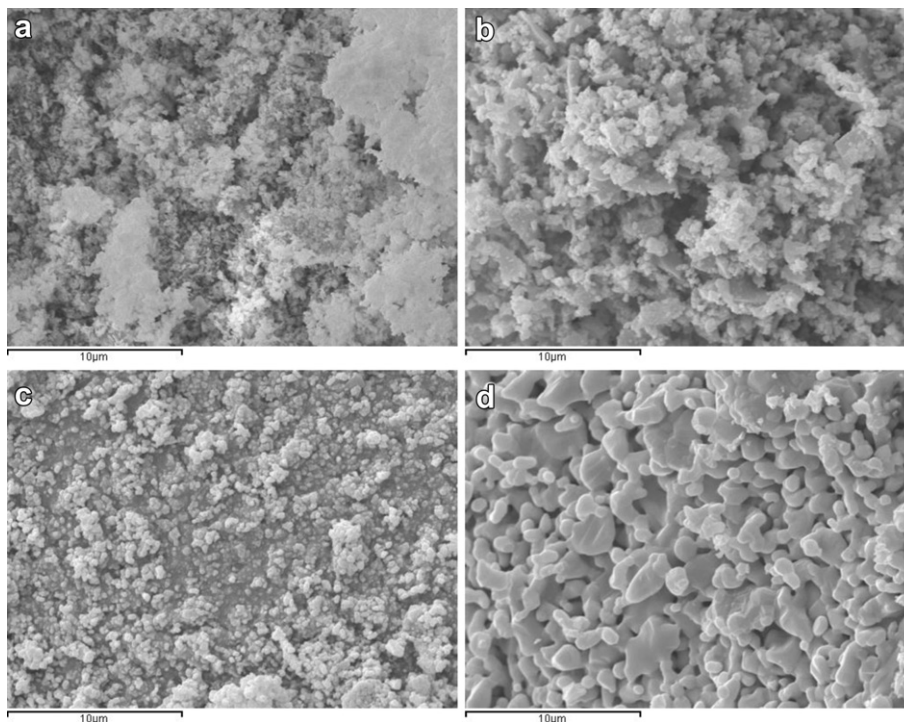
Fig. 2. Comparison of the initial particle size of (a) CG82 (as-sintered) and (b) LSM (as-received) and the resulting powders after calcination at 1150 °C: (c) CG82 and (d) LSM.

Fig. 2a. Comparing, for instance, the particle size of the ceria-based CG82 material with the as-received LSM powder (d_{50} = 0.6–0.3 μm) it can be observed by SEM imaging (Fig. 2a and b) that particle size is much smaller for the ceria-based co-precipitated powders. In addition, and despite the fact that initial sintering temperature for the ceria-based compounds is lower than the commercial LSM (1000 °C), after a 1150 °C calcination step, LSM powder has bigger and more sintered grains than ceria-based CG82 powder (Fig. 2c and d) indicating the higher sintering activity of LSM material compared to the co-precipitated ceria compound. On the contrary, ceria-based CG82 material seems to produce smaller grains, with respect to LSM, after treatment at high temperature even when the initial sintering temperature is low (800 °C).

Regarding this particle size evolution it should be assumed that the bigger LSM particles will become covered by smaller ceria-based ones in a non-well distributed composite. However, SEM images of several LSM-ceria composite cathodes (Fig. 3) revealed that particle size is similar for both materials (LSM and ceria-based) after sintering together at 1150 °C. Therefore the sintering of composite components that were calcined together is not as pronounced as when materials are sintered separately. This fact enables that mixtures of those materials have well distributed and connected

particles and the fabricated composite cathodes can maintain proper conducting paths and enough porosity for SOFC cathode purposes. Spatial constraints favored by the good mixing of LSM and doped-ceria phases in the composite cathode allow preventing particle agglomeration and coarsening of the electrode materials. Therefore both materials achieve similar particle size when calcined together. In addition, the possible presence of small nanoparticles of ceria-compounds (Fig. 2c) on the surface of bigger LSM grains might be beneficial from the point of view of the cathode performance, as reported for both LSM-YSZ [11] and GDC-impregnated LSM [12]. This could be a further optimization step, which would entail a final infiltration step of the previously sintered composite cathode.

3.2. DC-conductivity characterization

Electrical conductivity of ceria-based materials in air materials is shown in Fig. 4a at several temperatures. As described for several experimental works [13,14] on $Ce_{1-x}Gd_xO_{2-\delta}$ system, it can be observed that the total conductivity for CG91 is lower than for CG82 (Fig. 4a). The conductivity enhancement achieved by Gd^{3+} addition on the ceria fluorite lattice arises from the ionic conductivity introduced by intrinsic vacancies formed to maintain the
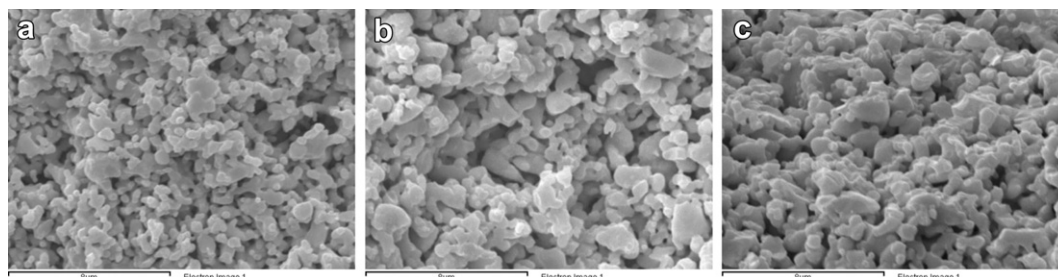

Fig. 3. SEM images of several composite cathodes sintered at 1150 °C: (a) CG82-LSM, (b) CG91-LSM and (c) CGBi-LSM.
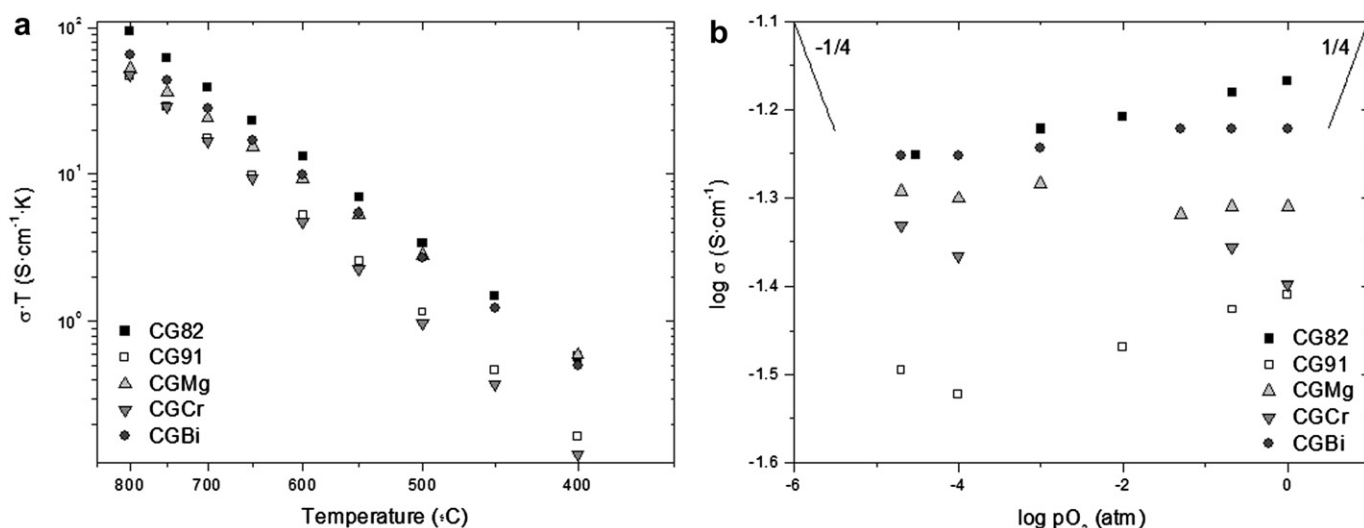
Fig. 4. Conductivity of ceria-based materials (a) at different temperatures in air (Arrhenius arrangement) and (b) in different oxygen partial pressures at 800 °C.

electroneutrality in the structure. Nevertheless, the best ratio for CeO_2–Gd_2O_3 solid solution is still not clearly defined for solid oxide fuel cells applications [15–18] since it depends on the proposed limiting conductivity mechanism. The co-doped materials of the present study with the general formula $Ce_{0.8}Gd_{0.1}X_{0.1}O_{2-\delta}$ have a cerium and gadolinium molar content in between CG82 and CG91. Surprisingly, the conductivity of these co-doped ceria materials (Fig. 4a) lies in between the values observed for 20% and 10% Gd-doped ceria, i.e., CG82 and CG91. The total conductivity of these co-doped materials is high enough for SOFC cathode applications since CG82 and CG91 conductivity fits with the SOFC application requirements.

Among the different co-doped materials, those based on bismuth (CGBi) and magnesium (CGMg) have similar conductivities. These conductivity values are close to those obtained for CG82 material at lower temperatures (Fig. 4a). On the other hand, CGCr composition has lower conductivity than the other two co-doped materials and it is even lower than CG91 compound when temperature decreases. Therefore it is possible to reduce gadolinium and/or cerium content in ceria–gadolinia materials without significantly decreasing the electrical total conductivity. This partial replacement of the gadolinium or cerium by other elements would make possible to cut production costs whereas both electrochemical and catalytic activity are not significantly affected.

In addition to the conductivity measurements performed in air, different oxygen partial pressure atmospheres were used for measuring the total conductivity of these materials (Fig. 4b) at 800 °C. The studied range of pO_2 includes both oxidant (0.21–1 atm) and moderately reducing atmospheres (10^{-5}–0.21 atm), in where Ce^{4+} does not reduce to Ce^{3+}. It has been demonstrated that Ce^{4+} reduction starts at oxygen partial pressures lower than 10^{-10} atm [19–22]. Conductivity values in this oxygen partial pressure range (Fig. 4b) seem to be independent on pO_2 for all the materials, and consequently p-type conductivity is negligible. Therefore, conductivity of these ceria-based materials is mainly ionic in these oxidizing conditions. It seems not possible to promote the electronic conductivity either in the bulk or in the grain boundary through the chosen doping strategy on the ceria-based fluorite structure.

3.3. Cathode testing on symmetric cells

The enhancement of the electrocatalytic properties of LSM cathode after mixing with ceria-based materials is shown in Fig. 5.

Electrode polarization resistance (R_p) values were obtained from electrochemical impedance spectroscopy measurements on symmetrical cells, fabricated with different LSM-ceria-based composite cathodes. The chosen LSM to ceria-based ratio (in weight) is 50/50 because it has been reported as the optimum [12] for SOFC LSM-based cathodes purposes. Irrespective of the ceria-based composition, the corresponding polarization resistance of the resulting composite electrode is lower than single LSM electrode at any tested temperature. This fact confirms that the addition of ion conducting paths (ceria-based percolating network) allows extending the TPB area into a certain thickness of the electrode. Indeed, the presence of ionic-conducting phase on LSM-YSZ state-of-the-art composite cathode also introduces ionic paths and increases TPB sites thus reducing the electrode polarization resistance (Fig. 5) compared to single LSM cathode. As previously explained [5,6], using ceria-compounds instead of YSZ materials could also increase the composite cathode electroactivity. As a consequence, the measured electrode polarization resistance for ceria-based composites is lower than for LSM-YSZ cathodes as observed in Fig. 5.
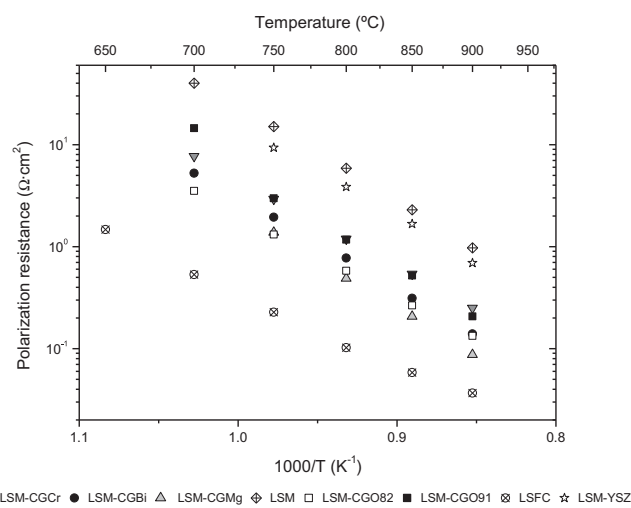

Fig. 5. Electrode polarization resistance of LSM-ceria-based composites and the single LSM electrodes at different temperatures (Arrhenius arrangement). LSFC and LSM-YSZ are shown for comparison.
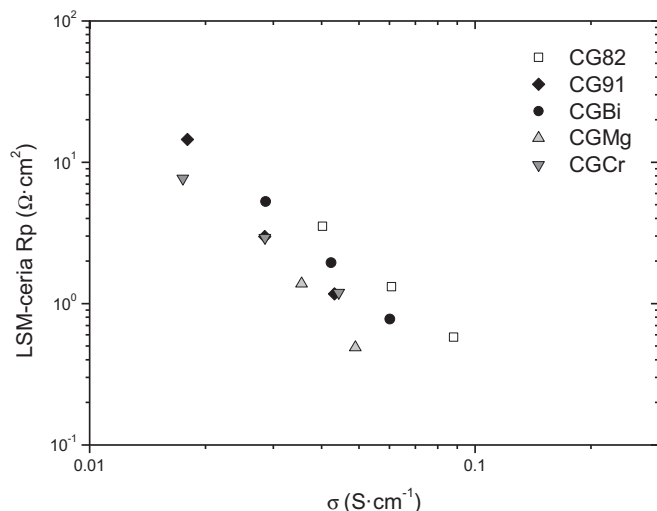
Fig. 6. Polarization resistance as a function of conductivity at three different temperatures (700, 750 and 800 °C).

Electrode polarization resistance values for the LSM-co-doped-ceria material composites lie in between LSM-CG82 and LSM-CG91 electrodes (Fig. 5), as previously observed for the electrical conductivity measurements of single ceria-doped materials (Fig. 4a). The best composite electrode regarding Rp values (Fig. 5) is the LSM-CGMg cathode at any tested temperature. It also presents lower electrode polarization resistances than the LSM-CG82 cathode at higher temperatures (800–900 °C). Nonetheless, electrode resistance of LSM-CGMg increases with decreasing operating temperatures, i.e., this cathode presents high activation energy. This performance worsening may be ascribed to the low oxygen vacancy association at lower temperatures. Chromium- or bismuth-co-doping does not improve the electrochemical reaction for oxygen reduction with respect to the LSM-CG82 composite.

Moreover, it can be inferred from Fig. 5 that all ceria-based material composites exhibit higher polarization resistances than the well-established high-performing LSFC cathode (tested on the same symmetrical cell electrolyte and experimental setup) but lower Rp than the single LSM electrode. Blending ionic materials (CGMg, CGBi, CGCr and Gd-doped ceria) with LSM allows increasing the concentration of TPB sites as previously reported for the CG82/LSM and CG91/LSM composites. However, the extension of the active zone for the oxygen reduction reaction in these composites is still restricted to TPB points and not the whole electrode surface area, as for LSFC mixed ionic-electronic conducting (MIEC) electrode. However, composite microstructure of the present ceria-based electrodes could be further optimized in order to approach the corresponding performance of MIEC cathodes [12,13,23].

Fig. 6 represents the polarization resistance of LSM-ceria-based composites as a function of ceria-based material conductivity at three temperatures (700, 750 and 800 °C) for all tested electrodes. In general, there exists a trend manifesting that the resistance decreases with increasing conductivities for selected cathode composites. However, all data points do not fall in the same (straight) trend line, which suggests that other factors are affecting the polarization resistance such as surface reaction activity, interfacial resistance, electrode microstructure, etc.

The high density degree of CG82-Co electrolyte [2,10] and the thickness of all porous electrode layers ($\sim$35 μm) can be inferred from the SEM images recorded on symmetrical cells fracture cross-section (Fig. 7). Electrodes are apparently very well attached to the electrolyte upon sintering in air at 1150 °C. Moreover, the grains of the two materials of the composite are well connected and distributed. Despite the fact that the initial particle size of the different doped-cerias varies significantly (Table 1 and Fig. 2a), a similar particle size distribution is observed for all electrodes, i.e., when they are mixed and sintered together with LSM (Figs. 3 and 7).

3.4. Impedance spectroscopy modeling

In the previous section, the results were analyzed in terms of the electrode polarization resistance obtained from electrochemical impedance spectroscopy measurements. As an example of such obtained data, Fig. 8a represents the Nyquist plot for the different LSM-ceria-based composites while Fig. 8b shows the corresponding imaginary Bode plot, both at 800 °C in air. Spectra in Fig. 8a correspond to the sum of both identical electrode contributions from symmetrical cells and from it the electrode polarization resistance can be calculated. In addition, data presented in Fig. 8 could also be fitted to an equivalent circuit comprising three ZARC elements, as named [24] by J. R. McDonald, in series with an inductance (from wiring) and a pure resistance, which originates mainly from current collection and electrolyte resistance. In Fig. 8a the value corresponding to the pure resistance (R) has been subtracted for all data series whereas the equivalent circuit is presented in the inset of Fig. 9. The pure resistance (R) slightly varied among samples because of current collecting and contact resistances.

Fitting values of spectra in Fig. 8, regarding to resistance, constant phase element parameters (Q_0 and n) and corresponding summit frequency of ZARC elements, are presented in Table 2, in which the area-corrected resistance values for single electrode contribution are presented. Taking into account the calculated summit frequency (as the inverse product of the resistance times the equivalent capacitance of the constant phase element [25]), two processes occur at similar relaxation times at high frequencies (A and B) and the other one at relatively low frequencies (C).

Electrochemical impedance response of electrodes based on LSM-YSZ composites has been described to possess up to five
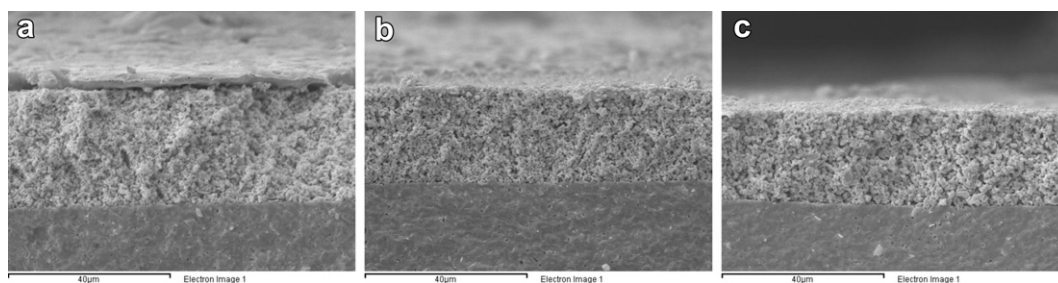

Fig. 7. Cross section SEM images of (a) CGCr-LSM, (b) CG82-LSM and (c) CG91-LSM electrodes on a dense CGO-Co electrolyte. The upper layer seen in (a) corresponds to the gold current collecting mesh.
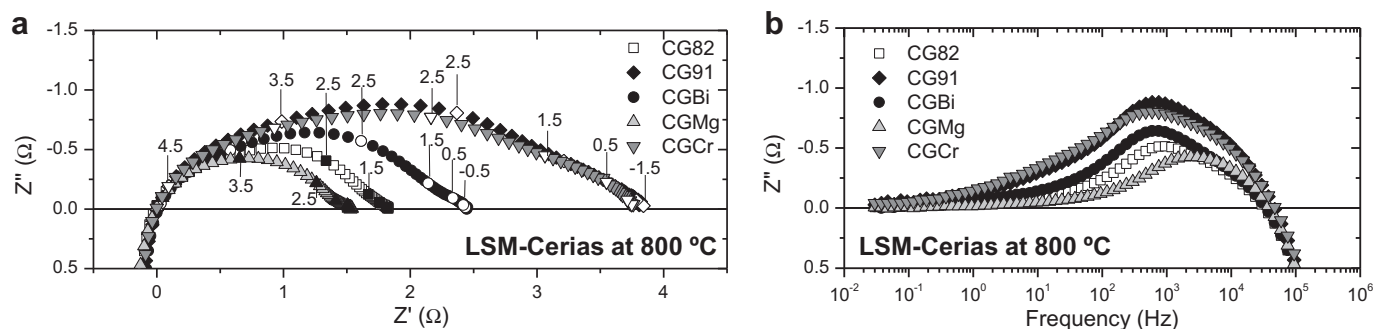
Fig. 8. Electrochemical impedance spectra of symmetrical cells with different LSM-doped-ceria electrodes at 800 °C in air: (a) Nyquist and (b) imaginary impedance Bode plots. Logarithm of selected frequencies is provided on the Nyquist plot.
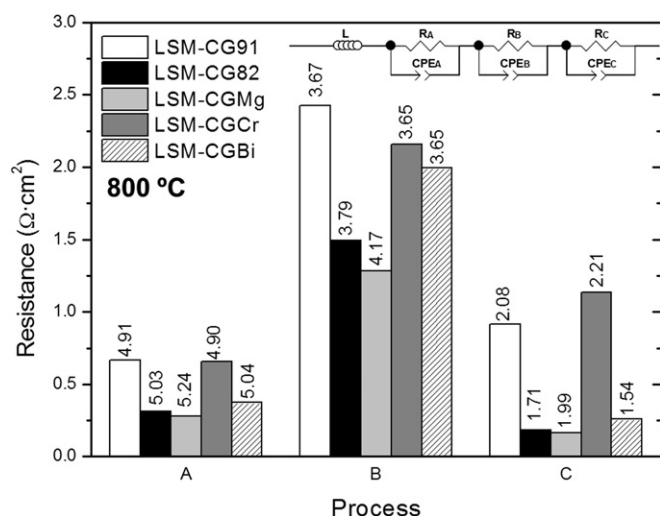

Fig. 9. Resistances corresponding to the different processes obtained by fitting the spectra of symmetrical cells at 800 °C in air according to the equivalent circuit $LR(R_AQ_A)(R_BQ_B)(R_CQ_C)$ shown in the inset. The corresponding logarithm of summit frequency is indicated on top of each bar.

contributions [26]. Nonetheless, three different electrode processes [27] named A, B and C seem to be the most predominant in Fig. 8 spectra. According to the possible processes [26–28] occurring in ceramic–ceramic composite cathodes for oxygen reduction reaction and the proposed model (Fig. 9) and results (Table 2), the two high frequency processes (named A and B) can be related to (1) transference of the oxygen intermediates/oxide ions or electrons

[29–31] between ceria and LSM particles; and (2) their transport through the ceria-based particles of the composite towards the electrolyte. On the other hand, the low frequency (LF) contribution (named C) is related to the dissociative adsorption, dissociation and transfer of species at TPB coupled with the surface diffusion, similar to the processes occurring in mixed ionic and electronic cathodes. The last assignment is supported on the exponent values close to 0.5 of the constant phase elements (n_C) (Table 2). Therefore the ZARC configuration could also have been modeled by a diffusion element [32] like a Gerischer or a Warburg [33,34]. However, in order to directly analyze the contribution of the resistance of each process to the total electrode resistance, it has been decided to model this contribution using a ZARC element.

In Fig. 9 resistance values for each fitted process are compared. Composite cathodes based on CG82 and CGMg showed resistance values lower than CG91- and CGCr-based composites for all three (A, B, C) processes. For LSM-CGBi cathode, the resistance assigned to process B seems to limit the whole cathode performance (Fig. 9) even when the other two contributions (A and C) have relatively low values. CGMg-based cathode presents the lowest LF resistance and this improvement of the surface processes should be related to both (1) the higher surface concentration of oxygen vacancies/ active (adsorption) sites in the oxygen reduction mechanism; and (2) the alkali character of the Mg cation, which improves the molecular oxygen adsorption. On the contrary, the highest LF contribution is observed for CG91 and CGCr. This could be caused by the lower surface concentration of oxygen vacancies and, in the particular case of CGCr, some detrimental effect of Cr species on the ceria surface and TPB sites.

The nature of limiting processes at the highest frequency range (A and B) cannot be unambiguously established. However, assuming that total conductivity at 800 °C for all doped cerias is

Table 2
Fitting parameters obtained for each LSM-ceria-based composite at 800 °C in air. R is the resistance, Q_0 and n are the constant phase element parameters and ω the summit frequency of each ZARC element, respectively. Capital letters (A, B, C) indicate the process according to the proposed electrical equivalent circuit.

Fit	Units	LSM-CG91	LSM-CG82	LSM-CGMg	LSM-CGCr	LSM-CGBi
R_A	Ω cm^2	0.21	0.10	0.09	0.21	0.12
Q_{0A}	S s^{-n}	5.26×10^{-5}	4.99×10^{-5}	1.08×10^{-5}	6.34×10^{-5}	1.21×10^{-4}
n_A	–	0.91	0.96	1.00	0.90	0.86
ω_A	Hz	8.10×10^4	1.08×10^5	1.74×10^5	8.00×10^4	1.10×10^5
R_B	Ω cm^2	0.77	0.48	0.41	0.69	0.64
Q_{0B}	S s^{-n}	9.62×10^{-4}	1.01×10^{-3}	5.80×10^{-4}	1.30×10^{-3}	1.28×10^{-3}
n_B	–	0.72	0.75	0.75	0.70	0.71
ω_B	Hz	4.65×10^3	6.10×10^3	1.47×10^4	4.47×10^3	4.49×10^3
R_C	Ω cm^2	0.29	0.06	0.05	0.36	0.08
Q_{0C}	S s^{-n}	8.23×10^{-2}	6.45×10^{-1}	4.26×10^{-1}	5.11×10^{-2}	4.52×10^{-1}
n_C	–	0.54	0.54	0.58	0.56	0.61
ω_C	Hz	1.21×10^2	5.12×10^1	9.82×10^1	1.63×10^2	3.47×10^1

similar (Fig. 4a), high frequency limitations should originate principally from the cathode microstructure [27], i.e., effective paths for oxygen ions/intermediates or electrons transfer are limited. Additionally, the potential role of grain boundary oxygen resistances of these ceria-based compounds [19] cannot be excluded, especially at lower temperatures.

On the whole, a high concentration of trivalent/divalent dopants (e.g. Gd^{+3} and Mg^{+2}), in the ceria lattice benefits the oxygen vacancy formation and the related electrode processes, at different frequency ranges, are enhanced due to the promotion of adsorption/dissociation steps, but also by the improvement in surface and *bulk* diffusion processes. On the contrary, the addition of multivalent chromium or gadolinium-isovalent bismuth has a detrimental effect on the global polarization resistance of the composite electrode. As a consequence, all three limiting processes analyzed and modeled here appear to be highly related one to each other.

4. Conclusions

Several ceria-based materials have been properly synthesized by co-precipitation method. Electrical conductivity of $Ce_{0.8}Gd_{0.1}X_{0.1}O_{2-\delta}$ (X = Gd, Cr, Mg, Bi, Ce) materials has been proved to be sufficient for SOFC applications. Specifically, the electrochemical properties of several $LSM-Ce_{0.8}Gd_{0.1}X_{0.1}O_{2-\delta}$ composite electrodes have been analyzed in symmetrical cells. In general, polarization resistance decreases with increasing ceria-based materials total conductivities. Among different co-dopants, Mg seems to enhance both the oxygen ion transferring and the surface processes for oxygen reduction. The addition of chromium and bismuth to the ceria-gadolinia-based materials seems not to improve the LSM-composite cathode performance. Nevertheless, performance and conductivity of these new co-doped composite materials as SOFC cathodes is not significantly higher than $Ce_{0.8}Gd_{0.2}O_{2-\delta}$ material. The use of the Mg-Gd-co-doped ceria may be viable due to economic reasons, regarding the price of cerium and gadolinium raw materials. Future work should address the optimization of the electrode microstructure through the variation of the starting particle size of both phases and the final electrode sintering temperature. Indeed, the improvement of the microstructure will affect the concentration of TPB sites, the resistance ascribed to *bulk* and surface oxygen-ion transport but also the rate of surface reaction processes and gas transport through the pore system.

Acknowledgements

Appendix A. Supplementary material

Supplementary data related to this article can be found at http://dx.doi.org/10.1016/j.jpowsour.2012.09.060.

References

[1] S.C. Singhal, K. Kendall, High Temperature Solid Oxide Fuel Cells: Fundamentals, Design, and Applications, Elsevier, Oxford, 2003.
[2] M. Balaguer, C. Solis, J.M. Serra, J. Phys. Chem. C 116 (2012) 7975–7982.
[3] D. Stolten, Hydrogen and Fuel Cells: Fundamentals, Technologies and Applications, Wiley-VCH, Weinheim, 2010.
[4] F. Tietz, Ionics 5 (1999) 129–139.
[5] M. Balaguer, C. Solis, J.M. Serra, Chem. Mater. 23 (2011) 2333–2343.
[6] T.Z. Sholklapper, H. Kurokawa, C.P. Jacobson, S.J. Visco, L.C. De Jonghe, Nano Lett. 7 (2007) 2136–2141.
[7] N. Imanishi, R. Ohno, K. Murata, A. Hirano, Y. Takeda, O. Yamamoto, K. Yamahara, Fuel Cells 9 (2009) 215–221.
[8] X'Pert HighScore Plus Software, Philips Analytical B.V., Almelo, The Netherlands, 2006.
[9] D. Pérez-Coll, P. Núñez, J.C.C. Abrantes, D.P. Fagg, V.V. Kharton, J.R. Frade, Solid State Ionics 176 (2005) 2799–2805.
[10] A. Kumar, S. Babu, A.S. Karakoti, A. Schulte, S. Seal, Langmuir 25 (2009) 10998–11007.
[11] E.P. Murray, S.A. Barnett, Solid State Ionics 143 (2001) 265–273.
[12] S.P. Jiang, W. Wang, Solid State Ionics 176 (2005) 1351–1357.
[13] T. Zhang, P. Hing, H. Huang, J. Kilner, Solid State Ionics 148 (2002) 567–573.
[14] N.P. Brandon, D. Thompsett, Fuel Cells Compendium, Elsevier, Oxford, 2005.
[15] V.V. Kharton, F.M. Figueiredo, L. Navarro, E.N. Naumovich, A.V. Kovalevsky, A.A. Yaremchenko, A.P. Viskup, A. Carneiro, F.M.B. Marques, J.R. Frade, J. Mater. Sci. 36 (2001) 1105–1117.
[16] B.C.H. Steele, Solid State Ionics 129 (2000) 95–110.
[17] D.S. Jung, S.H. Lee, J.M. Han, H.J. Hwang, J.H. Lee, Y.C. Kang, J. Ceram. Soc. Jpn. 116 (2008) 969–974.
[18] V.V. Kharton, Solid State Electrochemistry: Fundamentals, Materials and Their Applications, Wiley-VCH, Weinheim, 2009.
[19] D.P. Fagg, S. García-Martín, V.V. Kharton, J.R. Frade, Chem. Mater. 21 (2009) 381–391.
[20] D.P. Fagg, I.P. Marozau, A.L. Shaula, V.V. Kharton, J.R. Frade, J. Solid State Chem. 179 (2006) 3347–3356.
[21] K.L. Duncan, Y. Wang, S.R. Bishop, F. Ebrahim, E.D. Wachsman, J. Appl. Phys. 101 (2007) 044906.
[22] C. Chatzichristodoulou, P.V. Hendriksen, A. Hagen, J. Electrochem. Soc. 157 (2010) B299–B307.
[23] V.A.C. Haanappel, J. Mertens, D. Rutenbeck, C. Tropartz, W. Herzhof, D. Sebold, F. Tietz, J. Power Sources 141 (2005) 216–226.
[24] J.R. Macdonald, Impedance Spectroscopy: Emphasizing Solid Materials and Systems, Wiley, New York, 1987.
[25] J. Fleig, Solid State Ionics 150 (2002) 181–193.
[26] M.J. Jorgensen, M. Mogensen, J. Electrochem. Soc. 148 (2001) A433–A442.
[27] M.J.L. Østergård, M. Mogensen, Electrochim. Acta 38 (1993) 2015–2020.
[28] E. Barsoukov, J.R. Macdonald, Impedance Spectroscopy: Theory, Experiment, and Applications, John Wiley and Sons, New Jersey, 2005.
[29] V.B. Vert, J.M. Serra, Fuel Cells 9 (2009) 663–678.
[30] V.B. Vert, J.M. Serra, Fuel Cells 10 (2010) 693–702.
[31] J.M. Serra, V.B. Vert, ChemSusChem 2 (2009) 957–961.
[32] http://www.consultrsr.com/resources/eis/diffusion.htm.
[33] M.E. Orazem, P. Shukla, M.A. Membrino, Electrochim. Acta 47 (2002) 2027–2034.
[34] M. González-Cuenca, W. Zipprich, B.A. Boukamp, G. Pudmich, F. Tietz, Fuel Cells 1 (2001) 256–264.